ELSEVIER

Atmospheric Research 82 (2006) 310 – 327

ATMOSPHERIC RESEARCH

www.elsevier.com/locate/atmos

Influence of aerosol particles from biomass burning on cloud microphysical properties and radiative forcing

E. Cattani [a,*], M.J. Costa [a,b], F. Torricella [a], V. Levizzani [a], A.M. Silva [b]

[a] *ISAC-CNR, Institute of Atmospheric Sciences and Climate, Via Gobetti 101, Bologna, I-40129, Italy*
[b] *Department of Physics and Évora Geophysics Centre, University of Évora, Évora, P-7000, Portugal*

Accepted 4 October 2005

Abstract

Aerosol from biomass burning has been shown to strongly modify cloud microphysical properties and cloud lifetime through the so-called "indirect effect." However, in the case of a lack of wet scavenging, it stays suspended for days to weeks and can be transported to considerable distances within an elevated layer above low-level cloud tops with minimal aerosol–cloud interactions. The observations carried out during the Southern African Regional Science Initiative (SAFARI) 2000 dry season field campaign often revealed the presence of an elevated biomass-burning aerosol layer above a semi-permanent stratiform cloud deck off the southern African coasts.

MODerate-resolution Imaging Spectroradiometer (MODIS) cloud products were used to investigate the existence of an aerosol indirect effect on convective clouds. Results are presented documenting cloud effective radius and cloud radiative forcing variations due to the presence of the aerosol during the development of convective clouds.

Radiative transfer simulations in the visible (0.8 μm, VIS) and near-infrared (1.6, 2.1 and 3.7 μm, NIR) wavelengths were instrumental in establishing the extent of the influence of a biomass-burning aerosol layer overlying a water cloud sheet on the MODIS satellite retrieval of cloud parameters, in particular the effective radius and the optical thickness. The radiative transfer simulations suggest that the presence of the aerosol induces a significant underestimation of the cloud optical thickness, whereas an underestimation of the retrieved effective radius is more pronounced in the retrieval that makes use of the 1.6 μm waveband than the 2.1 and 3.7 μm wavebands. The MODIS cloud products of 3 days of the SAFARI 2000 campaign were analyzed to determine whether the aerosol induced biases evidenced by the simulations also affect the operational cloud property retrieval.

Cloud parameters, in particular the effective radius, are usually employed as indicators of the occurrence of aerosol–cloud interaction according to the "indirect effect." However, these results highlight some of the difficulties associated with satellite retrievals of cloud properties and show the importance of an accurate sighting of the cloud and aerosol layer top and bottom heights in order to prevent erroneous detections of indirect effects.
© 2006 Elsevier B.V. All rights reserved.

Keywords: Aerosol–cloud interactions; Cloud parameter retrieval; Radiative transfer; Remote sensing

1. Introduction

In recent years, the interaction of clouds with aerosol particles has been investigated through modeling studies, in situ measurements, and remote sensing

* Corresponding author. Tel.: +39 051 6398060; fax: +39 051 639 8132.

E-mail addresses: e.cattani@isac.cnr.it (E. Cattani), mjcosta@uevora.it (M.J. Costa), f.torricella@isac.cnr.it (F. Torricella), v.levizzani@isac.cnr.it (V. Levizzani), asilva@uevora.it (A.M. Silva).

0169-8095/$ - see front matter © 2006 Elsevier B.V. All rights reserved.
doi:10.1016/j.atmosres.2005.10.010

observations (Suzuki et al., 2004, and references therein). Various types of sub-micrometer aerosols acting as cloud condensation nuclei are responsible for significant modifications of cloud properties through the so-called "indirect effect." Statistical analysis based on satellite observations have unveiled a significant correlation between cloud droplet size and small particle aerosol loadings on a global scale (Bréon et al., 2002), so that increases in aerosol concentrations are associated with smaller mean values of the cloud droplet radius. This in turn leads to an enhancement of the cloud short-wave reflectivity (Twomey, 1977). Moreover, the effects of pollution by sub-micrometer aerosol on cloud lifetime (enhancement) and on precipitation-forming processes (reduction) have been first observed by Rosenfeld (1999, 2000). The alterations of cloud properties as a consequence of the interactions with aerosols may alter significantly the radiative forcing with respect to cloud conditions in pristine atmospheric environments (continental or marine).

The large injections in the atmosphere of aerosol released by frequent forest and cropland fires all over the planet are considered to be one of the main contributors to such modifications of cloud properties (List, 2004). Apart from significant amounts of inorganic compounds such as sulphates, this type of aerosol also contains organic compounds and black carbon, a strong absorber of solar radiation that can greatly influence cloud formation and evaporation (Ackerman et al., 2000). In the absence of wet scavenging, biomass-burning aerosol can stay suspended in the atmosphere for days to weeks and be transported to considerable distances confined in elevated polluted layers (Keil and Haywood, 2003), which can be located above cloud top and separated from it. The presence of the aerosol layer above the cloud deck can significantly affect satellite retrievals of cloud properties (effective radius and optical thickness), because the retrieval algorithms do not take into account the aerosol layer, giving rise to an erroneous detection of the "indirect effect" (Haywood et al., 2004).

The aim of the present work is twofold. First, the MODerate-resolution Imaging Spectroradiometer (MODIS) cloud products from selected scenarios characterized by convective clouds developing in the presence of biomass-burning aerosol are used to detect and quantify the aerosol "indirect effect" on cloud particle effective radius and, consequently, on cloud radiative forcing. Second, a radiative transfer modeling exercise is carried out to quantify the effects of a superimposed biomass-burning aerosol layer on the cloud property retrieval. Then the MODIS-derived cloud effective radius product is analyzed for three selected case studies during the Southern African Regional Science Initiative (SAFARI) 2000 to determine whether the aerosol radiative effects resulting from the simulations come out also of the operational cloud property retrieval. The simultaneous presence of clouds and aerosol requires a very judicious approach to standard cloud and aerosol products that are routinely derived from satellite data, since they are in general retrieved by neglecting one of the two components (for instance, the aerosol loading) when characterizing the other (for instance, the microphysical cloud properties). In the case of heavy aerosol loadings, cloud masks may have difficulties in separating the two components (Martins et al., 2002). Further, cloud property retrievals that disregard the presence of aerosols may suffer from non-negligible errors (e.g., Haywood et al., 2004).

The next section describes the case studies. Section 3 details the methodology used to derive the cloud properties and to estimate the cloud radiative forcing and the respective results. The potential biases in satellite based retrievals of cloud optical properties that do not account for an intervening aerosol layer are presented in Section 4. Finally, conclusions are proposed in Section 5.

2. The case studies

A case of smoke transport originated from the biomass fires that raged across southern Africa in early September 2000 at the peak of the fire season was analyzed. The area (see Fig. 1) and time period (7–13 September) were selected so as to benefit of the data of SAFARI 2000, a multinational measurement campaign that took place in southern Africa in August and September 2000 (Swap et al., 2003; http://www.daac.ornl.gov/S2K/safari.html). The heaviest burning was located in western Zambia, southern Angola, northern Namibia, and northern Botswana, as documented by Fig. 1, where the locations of burnt areas for the 2 months are shown according to the Global Burned Area (GBA) 2000 project data derived from the medium-resolution (1 km) satellite imagery provided by the SPOT-VEGETATION system (Grégoire et al., 2003).

The meteorological context and the haze layer characterization during the SAFARI 2000 campaign are reported by Swap et al. (2003) and Stein et al. (2003). The major circulation types controlling the tropospheric aerosol transport in the subtropics at the end of the dry season are described by Garstang et al. (1996). The relevant aspects for the present work can be summarized as follows. (1) The 2000 dry season followed a period of heavy rainfall anomaly, associated

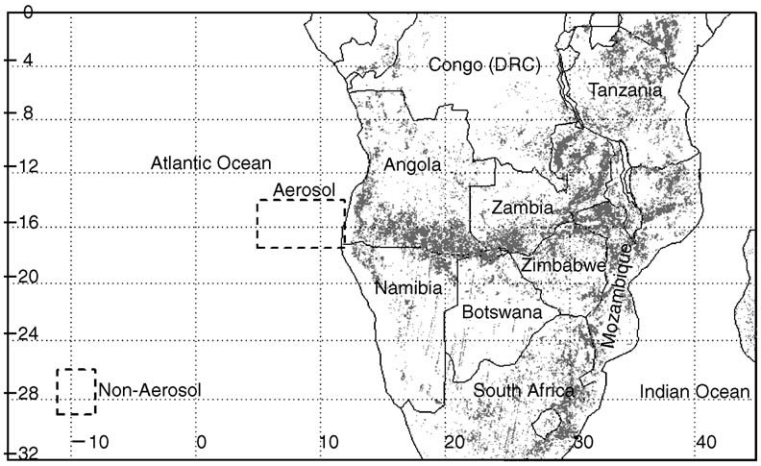

Fig. 1. Map of the area of the case studies. The analysis of the variations of the particle effective radius was conducted inside the two dashed boxes for two different situations: (1) clouds developing in the presence of aerosol (9 September 2000, 0950 UTC); (2) maritime clouds in clean atmosphere (10 September 2000, 1035 UTC). The locations of burnt areas in August and September 2000 are shown in gray according to the Global Burned Area (GBA) 2000 project data derived from the medium resolution (1 km) satellite imagery provided by the SPOT-VEGETATION system.

with la Niña phase of the El Niño–Southern oscillation. Such extremely "wet" climatic conditions fostered prolific vegetative growth and, hence, fire fuel for the dry season, which was characterized by biomass-burning episodes. Massive thick aerosol layers covered a large part of southern Africa as documented by the daily aerosol index (AI) maps of the Total Ozone Mapping Spectrometer (TOMS) (Torres et al., 1998) shown in Fig. 2 for the 5 days of the study. (2) During the campaign the atmospheric circulation was characterized by a high-frequency passage of westerly waves (every 4–5 days) and by the influence of tropical

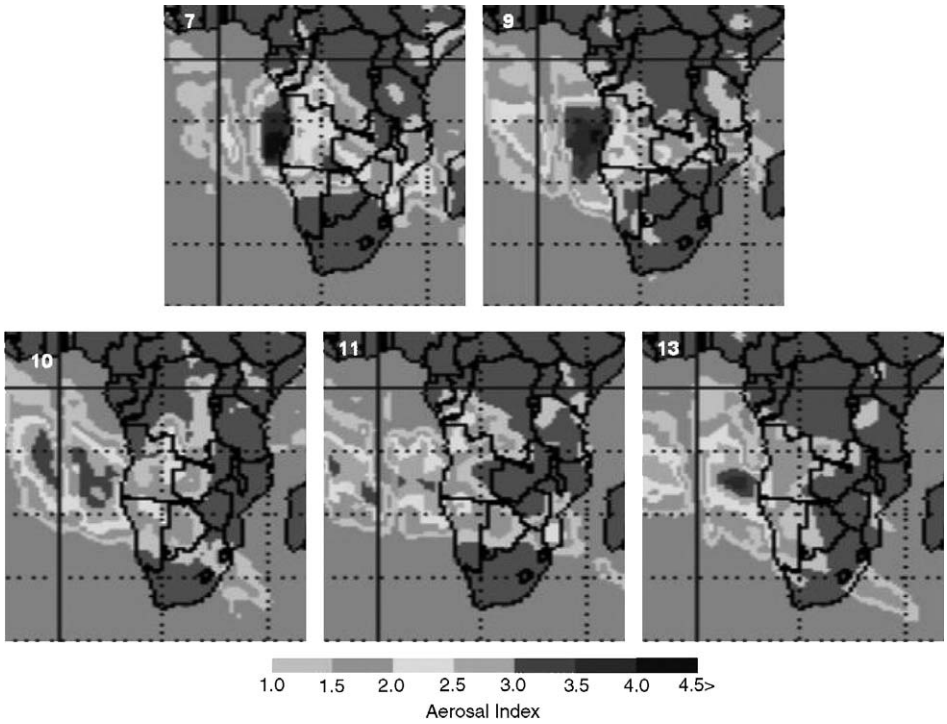

Fig. 2. TOMS aerosol index maps for the 5 days of the study.

easterly waves. These circulation types promote direct easterly and westerly streaming of particulate from southern Africa coasts. A noteworthy result of frequent disturbances was the disruption of the conditions of the classic anticyclonic gyre over the subcontinent, thereby decreasing the strength and frequency of high-pressure systems characterized by recirculation of air masses. (3) The strongly layered vertical structure of the lower troposphere in the region remained remarkably consistent with the vertical structure detected during the SAFARI 1992 observing period (Garstang et al., 1996) characterized by four absolutely stable layers. These layers serve as traps for trace gases and aerosols, thus serving in many cases as caps or upper boundaries for haze layers and controlling the transport over the continent. (4) The absence of precipitation and the low absolute humidity of the continental air masses over southern Africa during the dry winter became an obstacle in the detection of the effects of the biomass-burning aerosol on continental cloud formation. On the other hand, the aerosol transported over the ocean can mix with moist air masses and affect cloud properties. In situ analyses of aerosols, cloud condensation nuclei (CCN) and cloud droplet spectra during SAFARI 2000 confirm that biomass-burning aerosols produce very effective CCN, thus affecting cloud droplet size distributions (Swap et al., 2003).

The general meteorological conditions and peculiar phenomena occurring during the whole study period, lasting from 7 to 13 September, were examined as the necessary background frame. The occurrence of specific conditions during each event is supported by available coincident measurements (e.g., lidar measurements in Section 4) or by a more detailed description of meteorological conditions (as in the next section, dealing with aerosol indirect effects).

3. Biomass-burning aerosol indirect effects

This section examines the indirect effect that the biomass-burning aerosol may have on convective clouds through the analysis of cloud droplet radii.

Recent studies have demonstrated that aged aerosol particles from biomass burning can become hydrophilic enough to be activated as CCN at supersaturation conditions (Zuberi et al., 2005). The aerosol aging may occur by coalescence with soluble inorganic compounds such as H_2SO_4 and NaCl. Moreover, the oxidation by OH, O_3, SO_2, NO_x and HNO_3 forms surface polar groups responsible for the hydrophilic characteristics (Zuberi et al., 2005, and references therein). These latter justify the assumption that biomass-burning aerosol particles, activated as CCN, contribute to cloud development, modifying their microphysical characteristics.

The modification of the cloud microphysical parameters due to the interaction with the aerosol particles may induce variations in the cloud radiative forcing with respect to clouds forming in clean atmospheric conditions. These variations should be detected and quantified as precisely as possible.

3.1. Study area

The two areas of the MODIS overpasses selected for the analysis of cloud–aerosol interactions are shown as dashed boxes in Fig. 1. The MODIS Red–Green–Blue (RGB) composites for 9 and 10 September 2000 are shown in Fig. 3a and b. The aerosol plume emanating from the Angolan–Namibian coast shows up in Fig. 3a as a brownish haze merging with the cloud system extending over the south Atlantic Ocean with embedded brighter convective cells. The AI maps in Fig. 2 locate the aerosol plume and delimit its extension.

The box labeled "Aerosol" in Fig. 1 encloses an area of clouds probably developing in the presence of aerosol from biomass burning on 9 September 2000 0950 UTC. This hypothesis can be supported by several remarks.

Fig. 4 shows the synoptic map for 9 September 2000, as derived from the NCEP-NCAR 50 years reanalysis data available at NOAA (Kistler et al., 2001). The mean sea level pressure field is typical of a westerly wave condition. At 700 hPa, the wind vectors show a tendency to recirculation, according to Garstang et al.'s (1996) classification, and the pressure level is associated with the first absolute stable discontinuity (corresponding to about 3000 m asl). Aerosol was surely present at this elevated absolutely stable layer, transported by recirculation (see also Section 4.2), while direct transport at lower level is also known to occur. Thus, convective African coastal clouds have a high probability of processing aerosol loaded air through their base. Remote sensing of the modifications induced by aerosol on cloud hydrometeor size distributions is further complicated by the presence of the thick elevated aerosol layer, which can lay above the convective cloud top in its early development phases, when the vertical growth is not completed. However, the adopted Rosenfeld and Lensky (1998) classification and RGB display method demonstrate their robustness in detecting and analyzing aerosol indirect effects on cloud size distribution in such difficult conditions.

The "Non-Aerosol" box (10 September 2000, 1035 UTC) delimits an area of maritime clouds that

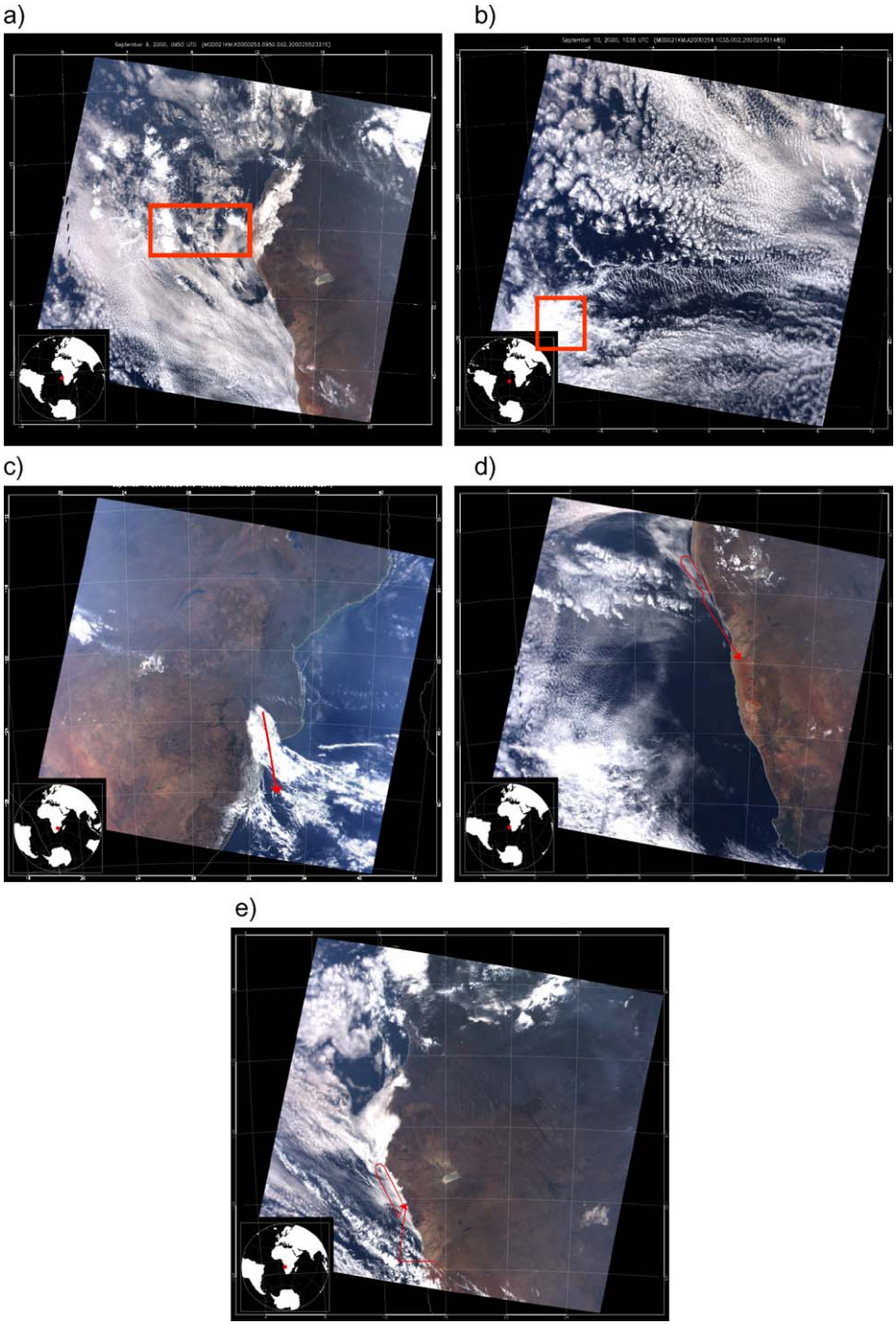

Fig. 3. RGB composites of the MODIS granules: (a) 9 September 0950 UTC, (b) 10 September 1035 UTC, (c) 7 September 0825 UTC, (d) 11 September 0940 UTC, and (e) 13 September 0925 UTC. The selected areas corresponding to the "Aerosol" and "Non-Aerosol" boxes in Fig. 1 are drawn in (a) and (b), respectively. The red broken lines in (c)–(e) locate the portions of the ER-2 aircraft flight trajectories characterized by the presence of clouds.

developed in a pristine atmosphere characterized by maritime aerosols, far from the biomass-burning influence zone.

The choice of the horizontal extent of the two study areas stems from considering trade-offs between two constraints: area large enough to contain

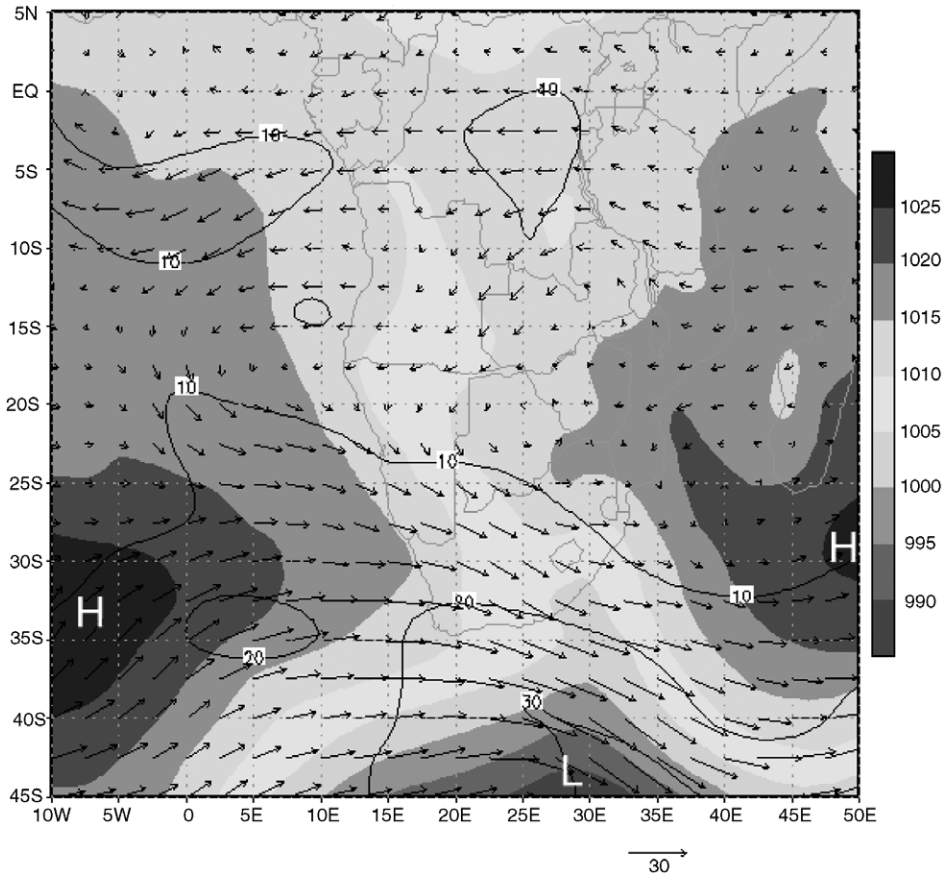

Fig. 4. Synoptic map on 9 September 2000: mean sea level pressure (hPa, shaded), isotachs (contours), and wind vectors at 700 hPa (m s^{-1}). Data derived from the NCEP-NCAR 50-year reanalysis.

clouds in different stages of their life cycle to ensure statistical significance, and, on the other side, not too wide so as to enclose clouds formed in a homogeneous air mass. The underlying assumption is that cloud top properties of a cluster of convective clouds having the top at different heights (i.e., at different stages of their vertical evolution) can be considered representative of the time evolution of the individual cloud element. The validity of this ergodicity assumption has been addressed by Lensky and Rosenfeld (2005).

The identification of convective pixels is done following the Rosenfeld and Lensky (1998) recommendations. A convective pixel is therefore detected when the following conditions are fulfilled: (a) visible reflectance (0.65 μm) greater than 0.4 and (b) infrared brightness temperature difference (BTD: $T_{11\,\mu m} - T_{12\,\mu m}$) smaller than $BTD_s + 1\,°C$, where BTD_s is the brightness temperature difference obtained from the precipitable water (PW) of a saturated atmosphere using the equation PW = 0.837 BTD (Eck and Holben, 1994).

3.2. Data and methods

The MODIS cloud products (King et al., 1997; Menzel and Strabala, 2002) are analyzed within the two selected boxes: top pressure, temperature (T) and phase (at $5 \times 5\,km^2$ resolution), cloud optical thickness (τ), particle effective radius (R_e) at three wavelengths (1.6, 2.1, and 3.7 μm), and water path (at 1×1 km^2 resolution). All products are geolocated, and geometry parameters are provided. Since cloud top temperature and effective radius data are used in the present analysis, the effective radius data are subsampled to match the spatial resolution of the cloud top temperature. The same procedure is applied to the cloud optical thickness data that are used in the computation of the cloud radiative forcing. The subsampling is done taking every fifth pixel along and across the scan, and it starts at the third pixel (along and across the scan).

The instantaneous cloud radiative forcing (ICRF) at the top of the atmosphere (TOA) was calculated from

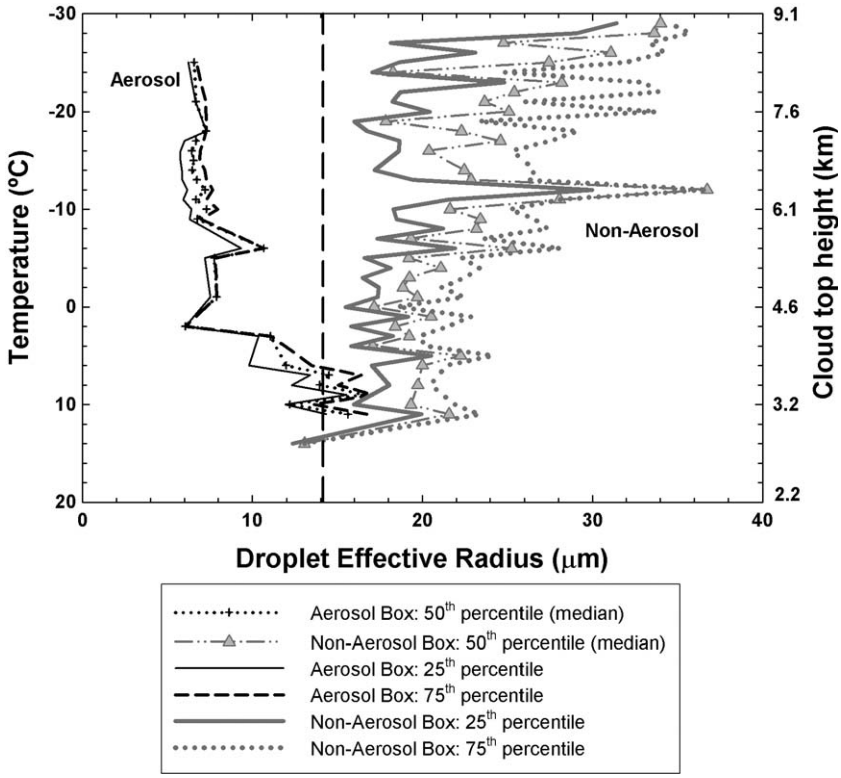

Fig. 5. Cloud top temperature as a function of droplet effective radius at 3.7 μm derived for two different situations inside the boxes of Fig. 1. The vertical dashed line indicates the 14 μm precipitation threshold described by Rosenfeld and Gutman (1994).

the net shortwave (N_{SW}) and longwave (N_{LW}) fluxes, according to the following equation,

$$\mathrm{ICRF} = (N_{SW} + N_{LW})^{\mathrm{cloud}} - (N_{SW} + N_{LW})^{\mathrm{nocloud}}$$

being the net fluxes given by the differences between the downward and upward fluxes, $N_{SW}=(SW\downarrow - SW\uparrow)$ and $N_{LW}=(LW\downarrow - LW\uparrow)$ (IPCC, 2001). A positive value of the ICRF indicates that the clouds cause a warming of the overall Earth–atmosphere system, whereas a negative value denotes a cooling of the system. Since the ICRF is estimated from the cloudy and cloud-free radiative fluxes, it strictly depends on the radiative properties of both clouds and surface (Ramanathan et al., 1989), which should then be accurately characterized.

The radiative fluxes were computed using FluxNet, a neural network version of the radiative transfer model (RTM) Streamer (Key and Schweiger, 1998). FluxNet is an extremely fast code for use in applications that require rapid and accurate radiative transfer calculations. Streamer, the RTM that trains the neural network of FluxNet, is based on the plane-parallel theory and uses the discrete ordinates solver DISORT (Stamnes et al., 1988). It is a medium spectral resolution model simulating the Earth–atmosphere radiative processes and the associated radiation budgets. The shortwave and longwave fluxes are computed in the 0.28–4.0 μm and 4.03–500 μm wavelength ranges using 24 and 105 bands, respectively, with variable width. The surface type is open sea water, characterized by the spectral reflectance model of Brieglieb et al. (1986). The surface temperature is obtained from the MODIS cloud product. The atmospheric gas absorption (H_2O, O_2, CO_2, O_3) is modeled using the Exponential-Sum Fitting of Transmission technique by Wiscombe and Evans (1977). Tropical atmospheric vertical profiles of temperature, pressure and water vapor are taken after Ellingson et al. (1991). The solar zenith angle values are those of each one of the MODIS pixels. Computations are performed for a solar zenith angle value of 20° that corresponds to the average value of the solar zenith angle of the MODIS pixels contained in the "Aerosol" labeled box. The cloud characterization, namely, phase, particle effective radius, optical thickness and top temperature, are derived from the MODIS cloud product. Aerosols are not considered in the flux calculations.

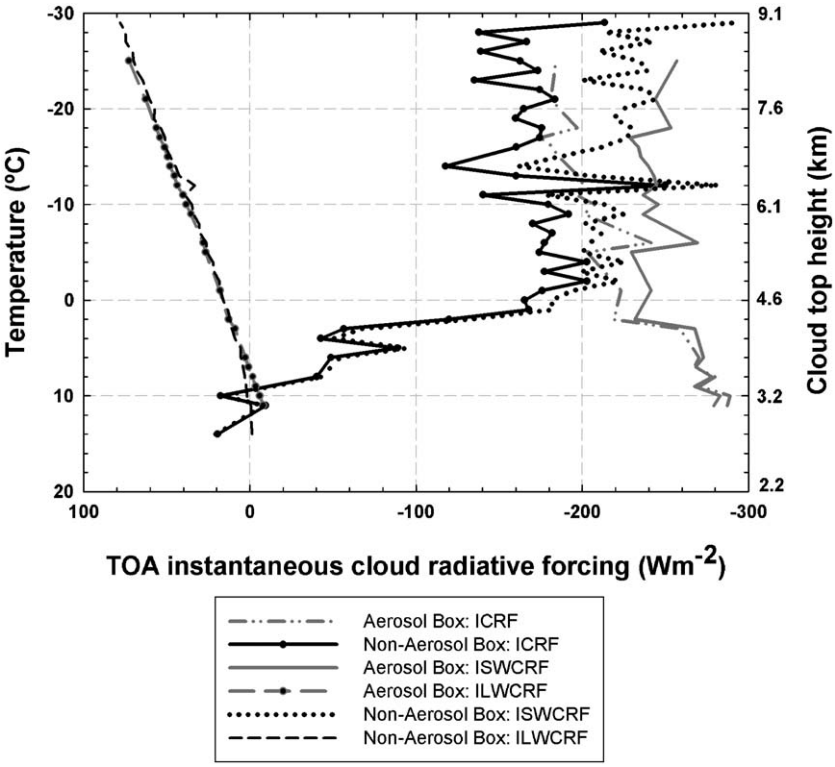

Fig. 6. Instantaneous SW, LW and net cloud radiative forcing at TOA for the dashed boxes in Fig. 1.

3.3. Classification scheme into microphysical zones and TOA radiative forcing

The relation between cloud top effective radius at 3.7 μm and cloud top temperature for developing convective clouds are instrumental in deriving information on microphysical cloud processes and, consequently, on precipitation formation processes (Rosenfeld and Lensky, 1998). The evolution of the droplet effective radius as the cloud top temperature decreases is plotted in Fig. 5. The temperature vs. R_e relation is calculated for the two boxes by retrieving an R_e distribution at each 1 °C step. The T vs. R_e curves of the 25th, 50th (median) and 75th percentile are displayed in the figure for clarity sake. The vertical dashed line represents the 14 μm precipitation threshold beyond which precipitation from convective clouds is likely to occur (Rosenfeld and Gutman, 1994).

Rosenfeld and Lensky (1998) studied ensembles of clouds with tops covering a wide range of temperatures and well distributed all over the globe. Based on the evolution of the droplet effective radius with temperature, they defined five vertical microphysical zones that may be identified during the development of a convective cloud system: (1) diffusional growth zone, characterized by very slow droplet growth rate; (2) coalescence growth zone, where droplets increase rapidly by coalescence at temperatures above freezing; (3) rainout zone, characterized by nearly constant values of R_e (between 20 and 25 μm); here, the droplet growth by coalescence is balanced by precipitation of the largest drops to lower heights and eventually rainfall from cloud base; (4) mixed phase zone, characterized by a large droplet growth rate at temperatures below 0 °C; (5) glaciated zone, which presents stable values of the effective radius, greater than those of the rainout zone. The five microphysical zones do not necessarily characterize all convective cloud systems. There are particular situations where some of these processes (zones) may be suppressed altogether (e.g., Rosenfeld and Lensky, 1998; Rosenfeld, 1999, 2000).

The curves corresponding to the "Non-Aerosol" situation in Fig. 5 exemplify some of the vertical zones mentioned before. First, in the lower atmosphere, cloud droplet size increased by coalescence with the effective radius reaching values of about 22 μm. A zone of rather stable R_e values between ~3200 and 5200 m follows, which is identified as the rainout zone. Finally, as temperature further decreases, mixed phase can be distinguished from −4 °C down below −12 °C, characterized by the large droplet growth rate, when the

glaciated zone seems to start. The 25th and 75th percentiles follow the trend of the median curve. The results for this case reasonably compare with results from highly maritime clouds (see Fig. 2 in Rosenfeld and Lensky, 1998).

The "Aerosol" curves in Fig. 5 represent the effective radius evolution for maritime clouds growing in the presence of smoke aerosols. Note that the curves are quite different from those of the "Non-Aerosol" situation. The cloud droplets, instead of growing, seem to diminish in size between 3100 and 4300 m. Afterwards, for temperatures below 0 °C, R_e is quite stable, with an exception around 5500 m, with values around 7 μm. The "Aerosol" curves slightly overcome the 14 μm precipitation threshold below 3700 m, but it is not clear whether rainout actually occurs. In summary, the various microphysical zones are not identified in such a profile, a fact that is most probably due to the severe effect that biomass-burning aerosols exert on cloud hydrometeors, leading to the inhibition of droplet growth. Rosenfeld (1999) shows a similar effect, demonstrating that Amazon smoke may stop the growth of cloud droplets with subsequent precipitation suppression.

Fig. 6 shows the ICRF at TOA together with the SW ICRF and the LW ICRF for the two test areas. Note that clouds developing in the aerosol-free atmosphere (solid black curve) present the less negative ICRF, increasing (more negative values) until around 0 °C and then slightly decreasing (less negative values) as the temperature decreases. As for the maritime clouds growing in the presence of aerosol (dashed dotted gray curve), ICRF has the highest (more negative) values, becoming progressively lower (less negative) with increasing height. The LW ICRF does not show significant differences among the various cases, since it is almost independent the cloud microphysical parameters. The SW ICRF presents the same trends as the ICRF, with the "Aerosol" case showing the more negative values. In the LW spectral region, clouds warm the system (positive values of LW ICRF), whereas in the SW the effect is the opposite. The net effect (ICRF) suggests that the convective cloud systems contaminated by the biomass-burning aerosol induce a more pronounced cooling of the Earth–atmosphere system. This is due to an increase of the cloud albedo as a consequence of the increased number of CCN and consequent overall diminution of droplet radius, which is in agreement with findings from several authors (Twomey et al., 1984; Rosenfeld, 1999, 2000; Bréon et al., 2002; Andreae et al., 2004).

4. Effects of overlying biomass-burning aerosol layers on cloud parameter retrievals

4.1. The radiative transfer model

Radiative transfer simulations at 0.8, 1.6, 2.1 and 3.7 μm were carried out assuming a stratocumulus cloud sheet with and without an overlying biomass-burning aerosol layer. The simulations serve the purpose of evaluating the sensitivity of reflectance at the operational MODIS retrieval wavelengths to the presence of the aerosol, and understanding its possible effects on the retrieval of τ and R_e since the MODIS algorithm is run disregarding the aerosol. Considering that the three case studies analyzed in Section 4.3 are over oceanic areas, the non-absorbing band at 0.8 μm was chosen among those of the MODIS cloud products (0.65, 0.8, 1.2 μm) in order to be consistent with the MODIS retrieval algorithm applied to oceanic pixels.

The simulated reflectances were computed using the RTM RSTAR4b (Nakajima and Tanaka, 1986, 1988; Stamnes et al., 1988), a 1-D, plane-parallel model for computing radiances at the VIS, NIR and infrared (IR) wavelengths with the simultaneous presence of water or ice clouds and an aerosol layer. The RTM can simulate radiances as measured by a satellite sensor using the response functions of its channels; monochromatic simulations are possible as well. The calculations are based on a combined discrete-ordinate/matrix-operator method, with the delta-*M* approximation for the representation of the phase function and the corrections for the singly scattered radiation. The delta-*M* approximation is suitable for representing the strongly asymmetric phase functions as those of clouds, characterized by a sharp forward diffraction peak and a number of secondary features (glory and bows). This is done via a series of low-degree Legendre polynomials, thus reducing the computational time and the storage space (Wiscombe, 1977; Levoni et al., 2001). According to this technique, the phase function can be approximated by the sum of a Dirac delta-function, representing the sharp peak, and a Legendre polynomial series, representing the phase function without the peak. Only a small number of polynomials are required since the Legendre series represents the "smooth" part of the phase function. The atmosphere is vertically divided into a user-defined number of homogeneous sublayers [up to a maximum number of 49 between the TOA (120 km) and the ground] and limited at the ground by a Lambertian surface. The vertical profiles of temperature, pressure and gases are taken from the atmospheric models of the Air Force Geophysical Laboratory

(AFGL) (Kneizys et al., 1988). The principal gaseous absorbers included in the RTM are water vapor, CO_2, O_3, N_2O, CO, CH_4, O_2, NO, SO_2, NO_2 and NH_3. Gas absorption is treated by means of a three-term *k*-distribution method (Fu and Liou, 1992), which prevents highly time-consuming line-by-line computations of the absorption coefficients, thus making the wavenumber integrations more agile for transmittance computations.

4.2. Radiative transfer simulations

The input parameters for the RSTAR4b RTM were taken from the SAFARI 2000 field campaign. The vertical distribution of the cloud and aerosol layers was deduced from Keil and Haywood (2003) who describe the typical scenario observed off the Angolan and Namibian coasts during September 2000. Thus, simulations targeted low-level stratiform clouds confined between 400 and 700 m and biomass aerosol located in an homogeneous layer between 1.8 and 3.7 km.

Clouds were regarded as a homogeneous vertical layer, characterized by a monomodal log-normal size distribution with a standard deviation $\sigma=1.42$ ($\ln\sigma=0.35$) (Haywood et al., 2004). The representative values for the cloud liquid water path measured during the SAFARI 2000 campaign ranged from about 7 to 60 g m^{-2} and $R_e \cong 7$–8 μm near cloud top (Keil and Haywood, 2003). Thus, the radiative transfer computations were carried out for $R_e=4$–20 μm and $\tau=2$–20.

A new aerosol type, more suitable to represent the radiative effects produced by the biomass-burning aerosol observed during SAFARI 2000, was included in the RSTAR4b aerosol data set. The extinction and absorption cross sections and the phase function of this aerosol were computed according to the Mie theory. Aerosol scattering properties were computed using wavelength-dependent real refractive index values (1.53 at 0.43 μm, 1.55 at 0.67 μm, 1.57 at 0.87 μm, and 1.60 at 1.20 μm), similar to those measured at the Aerosol Robotic Network (AERONET; Holben et al., 1998) Etosha-Pan site (Namibia) between 7 and 13 September 2000 and those reported in Yamasoe et al. (1998). A fixed value of the imaginary refractive index of 0.018*i* (Haywood et al., 2003a,b) was assumed. Measurements during SAFARI 2000 in Namibia have shown that the number size distribution of the aged regional haze can be fitted by a three-modal, log-normal distribution, whose parameters are summarized in Table 1. The first two smallest modes refer to the biomass-burning aerosol particles, whereas the third mode is likely to contain a significant amount of dust aerosol.

Table 1
Aerosol size distribution parameters used in the radiative transfer simulations. Data of Haywood et al. (2003a) are also reported as a reference

	Mode	Aerosol type	Number fraction	Mode radius r_0 (μm)	Standard deviation
Haywood et al. (2003a)	1	Biomass	0.9960	0.12	1.30
	2	Biomass	0.0033	0.26	1.50
	3	Dust	0.0007	0.80	1.90
	Mode	**Aerosol type**	**Volume fraction**	**Mode radius r_m (μm)**	**Standard deviation**
RSTAR4b	Fine	Biomass	0.89	0.15	1.3
	Coarse	Biomass	0.11	0.43	1.5

The third mode lacks completely in the very aged haze, presumably because of sedimentation. A bimodal log-normal volume size distribution was assumed as follows

$$v(r) = \sum_{i=1}^{2} C_i \cdot \exp\left[-\frac{(\ln r - \ln r_{mi})^2}{2(\ln\sigma_i)^2}\right],$$

where the C_i are weighting coefficients, and r_{mi} and σ_i the volume mode radius and standard deviation for each mode, respectively. It was not possible to include the third dust aerosol mode due to the constraints of RSTAR4b that does not work on multi-modal size distributions of different aerosol types. The values of the size distribution parameters are listed in Table 1. The volume mode radius values were computed from the number mode radius values reported in Haywood et al. (2003a), taking into account for each modes the relationship between the volume size distribution valid for spherical particles

$$v_i(r) = \frac{4}{3} \cdot \pi r^4 \cdot n_i(r)$$

and the corresponding number size distribution $n_i(r)$

$$n_i(r) = \frac{C'_i}{r} \cdot \exp\left[-\frac{(\ln r - \ln r_{0_i})^2}{2 \cdot (\ln\sigma_i)^2}\right]$$

and the consequent relation between the volume mode radius (r_{mi}) and the mode radius of the number size distribution (r_{0i})

$$r_{mi} = r_{0i} \cdot \exp[3 \cdot (\ln\sigma_i)^2].$$

The single scattering albedo and the extinction coefficients normalized at 0.55 μm resulting from the assumed setup of the aerosol layer are in good agreement with those of Haywood et al. (2004) as shown in Table 2. The same is not true for the asymmetry parameter values, in particular for the NIR wavelengths, which do not show

Table 2
Comparisons between the scattering properties of the biomass burning aerosol: single scattering albedo, extinction coefficient normalized at 0.55 μm, and asymmetry factor

	Wavelengths (μm)					
	0.55	0.63	0.87	1.63	2.13	3.7
Single scattering albedo (ω_0)						
Haywood et al. (2004)	0.91	0.88	0.86	0.78	0.78	0.75
RSTAR4b	0.91	0.90	0.88	0.84	0.81	0.73
Normalized extinction coefficient (K_{ext})						
Haywood et al. (2004)	1	0.78	0.38	0.10	0.08	0.04
RSTAR4b	1	0.79	0.42	0.12	0.07	0.02
Asymmetry factor (g)						
Haywood et al. (2004)	0.59	0.52	0.40	0.48	0.50	0.57
RSTAR4b	0.60	0.57	0.47	0.42	0.40	0.28

the expected wavelength dependence with a minimum at 0.87 μm. This effect is most likely due to the absence in the size distribution of the coarser dust aerosol mode. Finally, an aerosol optical thickness at 0.5 μm (τ_{aer}) value of 0.5 was adopted, according to the value used in Haywood et al. (2004). Area plots of time-averaged τ_{aer} values from MODIS revealed that this value of τ_{aer} can be considered representative of the aerosol load of oceanic areas off the Namibian and Mozambican coasts during September 2000.

Standard tropical atmospheric profiles and a Lambertian surface albedo of 0.05 were adopted for the simulations.

The simulated data at 3.7 μm did not include the thermal emitted component, as the solar reflected component is much more sensitive to the cloud droplet size variations and is therefore exploited by the cloud effective size retrieval algorithms (King et al., 1997; Nakajima and Nakajima, 1995).

The results of the RTM computations are shown in Fig. 7a–c. NIR reflectances are plotted as a function of the 0.8-μm reflectances; black filled circles represents cloud-only reflectances, while open diamonds those contaminated by the aerosol layer. Each solid curve refers to a different value of R_e and the dashed lines are curves with a constant value of τ. A nadir viewing geometry with a solar zenith angle of 0° is to be assumed since simulations performed at different sun–observer geometries do not reveal qualitatively different patterns. The scarce influence of the solar geometry on this kind of RTM simulations is also confirmed by the similarity of the present results with those of Haywood et al. (2004) for different solar geometries.

The presence of a partially absorbing aerosol layer above the cloud top induces a significant underestimation of τ, as suggested by the reflectance data at 0.8 μm that are diminished by the effect of the biomass-burning aerosol. The effect is more evident for high τ values but it shows up also at smaller τ. For example, the 0.8-μm reflectances computed for $\tau=20$ and including the aerosol layer are comparable with reflectances without the aerosol and $\tau=16$. Similarly, reflectances with aerosol and $\tau=10$ are similar to those computed without aerosol and $\tau=8$.

A decrease of the NIR reflectances is also documented in Fig. 7a–c, due to the absorption of the cloud scattered radiation by the biomass-burning aerosol layer. At the same time, the simultaneous decrease in the NIR and VIS reflectances can induce an underestimation of τ and an underestimation of the retrieved R_e that might be erroneously interpreted as an indirect effect of the aerosol on cloud particle size (Haywood et al., 2004). The reflectance at 1.6 μm including the aerosol and computed for $\tau=20$ and $R_e=12$ μm is comparable (see Fig. 7a) with the reflectance without aerosol for $\tau=16$ and $R_e=10$ μm. The effect is noticeable also for smaller τ values at 1.6 μm, e.g., the reflectance including aerosol computed for $\tau=10$ and $R_e=8$ μm that produces the retrieved values of $\tau=8$ and $R_e=6$ μm. NIR reflectances at 2.1 and 3.7 μm are only moderately affected by the aerosol and for $\tau \lesssim 10$, because of the greater τ_{aer} value at 1.6 μm (0.05) than at the other two wavelengths (0.03 and 0.01, respectively). Note the reflectance at 2.1 μm including aerosol with $\tau=8$ and $R_e=14$ μm (Fig. 7b), which is similar to that without aerosol and $\tau=6$ and $R_e=12$ μm.

4.3. The aerosol radiative effect on the MODIS cloud parameter retrieval

The evidence of the effect of a biomass-burning aerosol layer overlying a stratocumulus cloud on an actual cloud parameter retrieval from satellite radiance measurements was investigated using MODIS cloud products. R_e values at 1.6, 2.1 and 3.7 μm of three MODIS data granules acquired in different days during the SAFARI 2000 campaign were analyzed. Top and bottom heights of the cloud and aerosol layers were precisely located (resolution is 30 m vertical and 200 m horizontal) from the profiles of volume 180° backscatter coefficients measured by the Cloud Physics Lidar (CPL) (McGill et al., 2002, 2003) flying on board the NASA ER-2 high-altitude aircraft during the campaign (available at http://cpl.gsfc.nasa.gov/). The CPL can detect up to 10 different layers, distinguishing among planetary boundary layer, cloud layer and elevated aerosol layer. An example of such a data set of cloud and aerosol

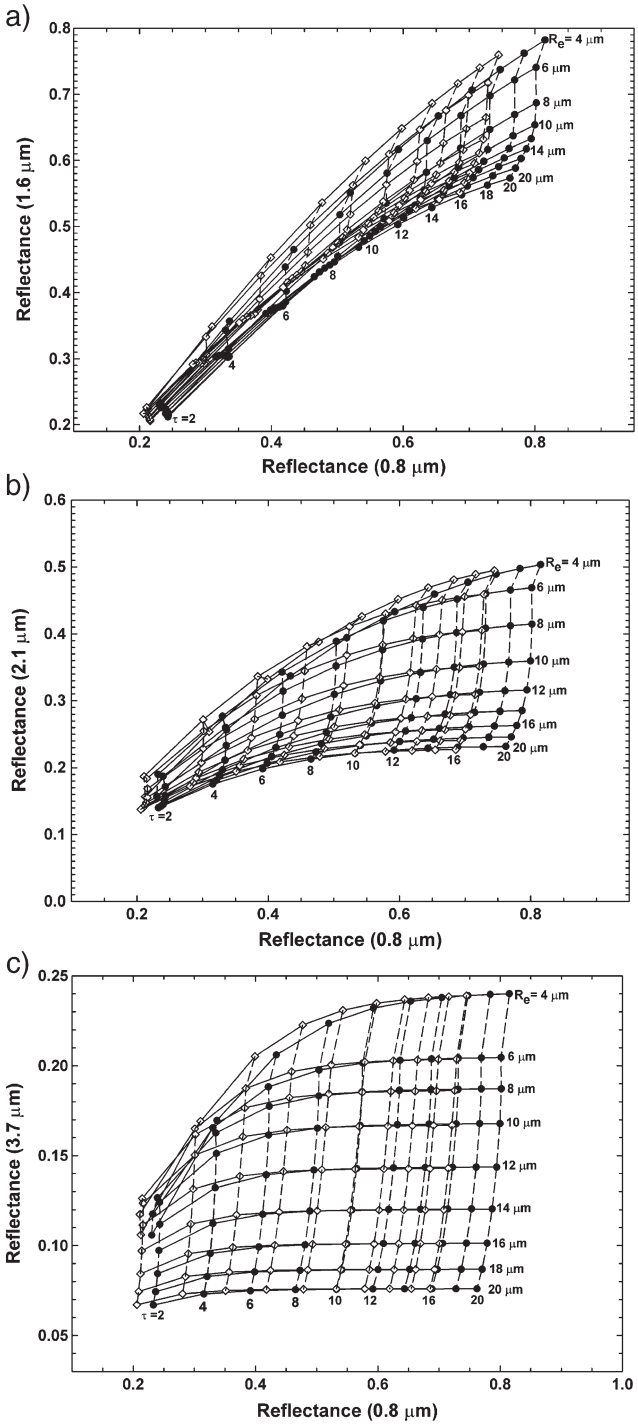

Fig. 7. (a) Simulated NIR (1.6 μm) and VIS (0.8 μm) reflectances as a function of R_e and τ. Black filled circles show the results without the aerosol, and open diamonds those including the biomass burning aerosol layer with $\tau_{aer}=0.5$. Computations refer to solar and satellite zenith angles of 0°. (b) Same as in (a) but for simulated reflectances at 2.1 μm. (c) Same as in (a) but for simulated reflectances at 3.7 μm.

boundaries for the 13 September 2000 was shown in Cattani et al. (2003). During SAFARI 2000 CPL measurements were validated against the ground-based Micro-Pulse Lidar Network (MPL-Net) and the NASA Ames Airborne Tracking 14-channel Sun photometer (AATS-14) operating on board the University of

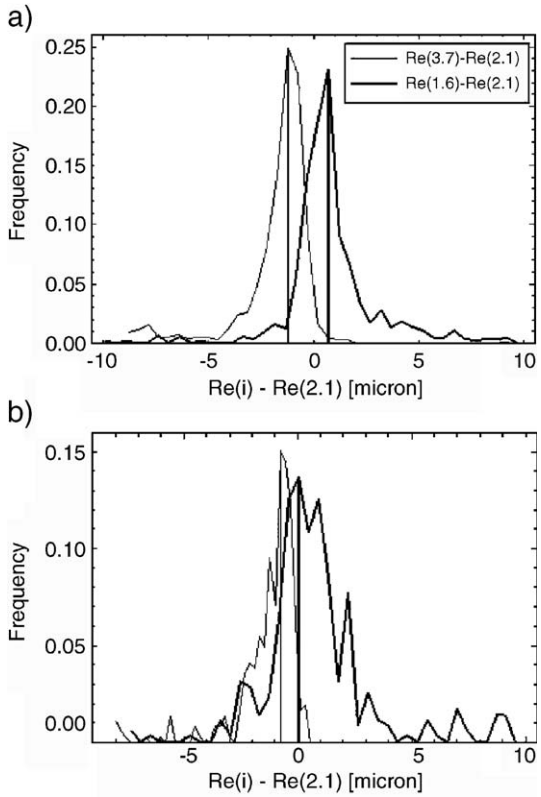

Fig. 8. 7 September 2000. Frequency distribution functions of the $R_e(1.6)-R_e(2.1)$ (thick line) and $R_e(3.7)-R_e(2.1)$ (thin line) values for the MODIS pixels a) not contaminated, b) contaminated by the aerosol. The vertical lines denote the modal values of the distributions.

Washington's Convair-580 research aircraft (McGill et al., 2003; Schmid et al., 2003). For each case study, only the CPL pixels containing a cloud layer were selected and the data where the magnitude of the aircraft roll exceeded 3° were considered invalid and excluded from the analysis. The RGB composites of the three selected MODIS granules in September 2000 are shown in Fig. 3c–e [(c) 7, 0825 UTC, (d) 11, 0940 UTC, and (e) 13, 0925 UTC] together with the ER-2 aircraft flight trajectory (red line) in cloudy conditions. Given a CPL pixel, the co-located MODIS pixel was detected (difference in latitude and longitude smaller than 0.01°) and classified as aerosol or non-aerosol contaminated according to the lidar detection/non-detection of the elevated aerosol layer above the cloud top. The inspection of the MODIS cloud phase product for the three case studies revealed the absence of ice clouds along the legs of the aircraft trajectories used for the MODIS pixel classification. For this analysis, only MODIS cloudy pixels with $\tau<20$ were selected to be consistent with the theoretical computations. CPL measurements were taken at (1) 1000 to 1041 UTC, (2) 0950 to 1110 UTC, and (3) 0900 to 1100 UTC. They were not perfectly time coincident with the three satellite granules, but the delay never exceeded a few hours, thus justifying the exploitation of the CPL data in the analysis of the MODIS cloud products.

The differences between R_e values retrieved at 1.6 and 3.7 μm and those retrieved at 2.1 μm, $R_e(1.6)-R_e(2.1)$ and $R_e(3.7)-R_e(2.1)$, were used to detect the signature of the aerosol radiative effect. According to the RTM simulations, the aerosol effect on the R_e retrieval should be pronouncedly wavelength dependent. Therefore, a decrease of $R_e(1.6)-R_e(2.1)$ values is expected due to the aerosol effect that causes an underestimation of the retrieved $R_e(1.6)$ values, whereas the differences $R_e(3.7)-R_e(2.1)$ should be only moderately influenced. The frequency distribution functions of the two differences are presented in Figs. 8–10. The statistical parameters of the frequency distributions (mode and median values) are reported in Table 3, together with the number of the MODIS aerosol-contaminated and aerosol-free pixels.

In the first case (Fig. 3c) the NASA ER-2 aircraft flew over a cloud system off the coast of Mozambique. During this portion of the flight, 360 pixels out of the

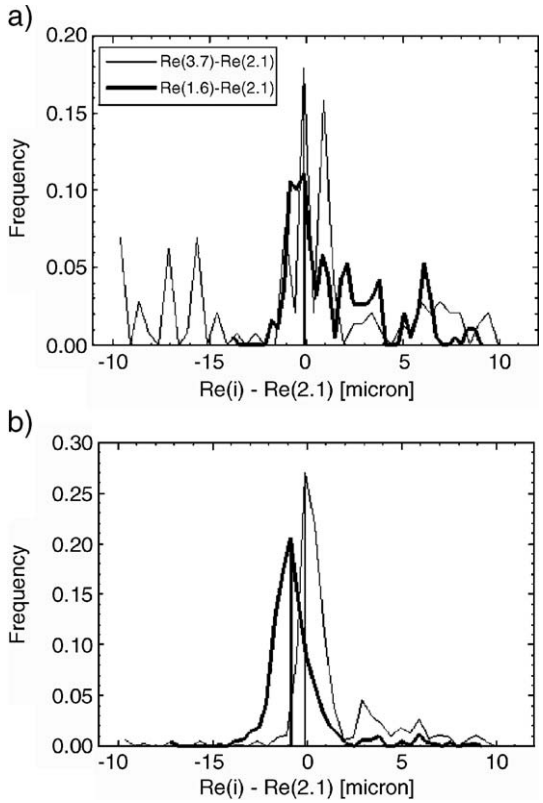

Fig. 9. Same as in Fig. 8 but for the 11 September granule.

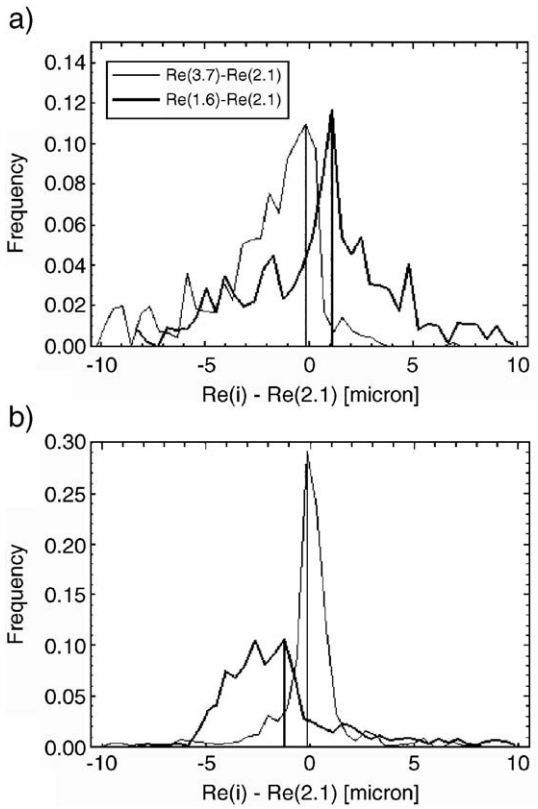

Fig. 10. Same as in Fig. 8 but for the 13 September granule.

1810 spatially coincident with the ER-2 trajectory were classified as aerosol contaminated. The frequency distribution functions of the $R_e(1.6)-R_e(2.1)$ (thick line) and $R_e(3.7)-R_e(2.1)$ (thin line) values are reported in Fig. 8 for aerosol-free pixels (Fig. 8a) and for those that were aerosol contaminated (Fig. 8b). The vertical lines indicate the modal values of the distributions. In this case, the presence of the aerosol layer has a moderate effect on the distribution functions, as demonstrated by the variations of the statistical parameters (Table 3). The $R_e(1.6)-R_e(2.1)$ distribution for the non-contaminated pixels shows a maximum at 0.67 μm that is shifted to 0.03 μm for the aerosol-contaminated ones. Moreover, the absence of a marked aerosol radiative effect is also demonstrated by the small decrease of the median values (from 0.78 to 0.64 μm), which means that no substantial shift of $R_e(1.6)-R_e(2.1)$ towards smaller or negative values is detected. Analogous conclusions can be drawn for the $R_e(3.7)-R_e(2.1)$ distributions, which do not show any statistically significant differences. However, note that the aerosol type and amount in this area are quite different from those of the Namibian coastal regions (Eck et al., 2003). Measurements during SAFARI 2000 at the Inhaca Island AERONET site (Mozambique, 26°02′S 32°54′E) revealed a substantial contribution from super-micrometer particles of marine aerosol and industrial pollution. The aerosol contributions from fossil fuel burning and industrial emission influence the aerosol mixture in this area, therefore also modifying the absorption characteristics. Moreover, τ_{aer} measurements from the Inhaca Island AERONET site showed a daily average value of about 0.2 for September 7 (Eck et al., 2003), a value significantly lower than that used in the RTM simulations. Only negative values are found for the non-contaminated $R_e(3.7)-R_e(2.1)$ differences (Fig. 8a) unlike the other non-contaminated distributions (Figs. 9a and 10a). These findings disagree with those by Platnick et al. (2003) about optically thick stratocumulus clouds characterized by slightly positive $R_e(3.7)-R_e(2.1)$ differences, though typically less than 1 μm. The corresponding non-contaminated distribution reported

Table 3
Statistical parameters of the frequency distribution functions of the $R_e(1.6)-R_e(2.1)$ and $R_e(3.7)-R_e(2.1)$ for the aerosol-contaminated and non-contaminated pixels

	Number of pixels	Modal values (μm)		Median values (μm)	
		$R_e(1.6)-R_e(2.1)$	$R_e(3.7)-R_e(2.1)$	$R_e(1.6)-R_e(2.1)$	$R_e(3.7)-R_e(2.1)$
7 September 2000					
Non-aerosol	1450	0.67	−1.23	0.78	−1.00
Aerosol	360	0.03	−0.77	0.64	−0.76
11 September 2000					
Non-aerosol	194	−0.14	−0.08	0.94	0.40
Aerosol	1409	−0.86	−0.08	−0.64	0.56
13 September 2000					
Non-aerosol	1262	1.07	−0.13	1.04	−1.31
Aerosol	2463	−1.26	−0.14	−1.78	0.27

in Haywood et al. (2004) also appear quite different, with a modal value near zero and the same occurrences of positive and negative $R_e(3.7)-R_e(2.1)$ differences.

The area overflown by the ER-2 on September 11 off the Namibian coast (Fig. 3d) was dominated by the presence of an aerosol layer above cloud top, as proved by the CPL measurements. 1409 aerosol affected pixels were found out of the 1603 MODIS pixels spatially coincident with the ER-2 trajectory. The aerosol contaminated and non-contaminated frequency distributions of $R_e(1.6)-R_e(2.1)$ and $R_e(3.7)-R_e(2.1)$ are presented in Fig. 9a and b. The aerosol is attributed a displacement of 0.72 μm (towards more negative values) of the modal value of the $R_e(1.6)-R_e(2.1)$ frequency distribution after comparing Fig. 9a with b, whereas the position of the peak (centered at −0.08 μm) of the $R_e(3.7)-R_e(2.1)$ distribution remains unchanged. At the same time, Fig. 9b shows a substantial decrease of the occurrences of positive $R_e(1.6)-R_e(2.1)$ values and a corresponding increase of the $R_e(1.6)-R_e(2.1)$ negative values up to −3 or −4 μm, as confirmed by the decrease of the median values from 0.94 to −0.64 μm.

The distributions of the differences on September 13 (Fig. 10a and b, 3725 MODIS pixels selected for the analysis, 2463 aerosol contaminated) uncover an evident aerosol radiative effect. The modal value of the $R_e(1.6)-R_e(2.1)$ frequency distribution is now shifted by 2.33 μm towards more negative values. It increases to 3.72 μm, if the secondary maximum at −2.75 μm of the aerosol-contaminated $R_e(1.6)-R_e(2.1)$ distribution is considered. Moreover, 50% of the aerosol contaminated pixels have $R_e(1.6)-R_e(2.1)$ values between −1.78 μm and −5 μm. Such differences are hardly explained by considering only the vertical distribution of R_e in the cloud, and not accounting for the effect of the biomass-burning aerosol (Haywood et al., 2004). The $R_e(3.7)-R_e(2.1)$ distribution of the non-contaminated pixels is centered near zero with a modal value of −0.13 μm, which is unvaried in the presence of the aerosol (−0.14 μm).

5. Conclusions

Cloud–aerosol interactions during SAFARI 2000 have revealed a decrease of the cloud droplets effective radius when smoke aerosol particles are present over the area. The evolution of cloud top temperature and effective radius of convective clouds in the area indicates that droplets in clouds that come in contact with biomass burning particles grow less. The corresponding ICRF reveals that "smoky" clouds reflect slightly more radiation to space than the "clean" ones.

However, besides the described true indirect effect, a spurious effect due to a superimposed elevated aerosol layer was detected, which was not considered by the MODIS retrieval algorithm.

The radiative effects produced by a biomass-burning aerosol layer overlying a stratocumulus cloud deck were investigated by means of radiative transfer simulations of radiances at 0.8, 1.6, 2.1 and 3.7 μm. The computations used a realistic description of the aerosol optical properties and of the vertical position of aerosol and cloud layers. The inclusion of an aerosol layer with $\tau_{aer}=0.5$ was shown to produce significant biases in the satellite based retrievals of cloud optical properties. Underestimations of τ range from 20 to 25%, whereas those of R_e are more pronounced at 1.6 μm than at the other NIR wavelengths and can lead to retrieval errors up to 25%.

The analysis of the aerosol effects on the MODIS cloud products, in particular R_e at the three NIR channels, did not produce as sharp results as those of the RTM simulations. The frequency distribution functions of the differences $R_e(1.6)-R_e(2.1)$ showed significant displacements of the modal value only for the case study of 13 September 2000. In this case, a shift of 2.33 μm towards smaller (more negative) values indicates an $R_e(1.6)$ underestimation due to the aerosol presence. Only very small variations of the modal values of the $R_e(3.7)-R_e(2.1)$ frequency distributions resulted from the MODIS data, as it was expected from the simulations, where the 3.7-μm radiances were the less affected by the aerosol.

The identification of the aerosol effect on R_e retrievals is further complicated by several factors. First of all, the classification of the MODIS pixels as aerosol contaminated or not may be questionable, due to the temporal delay between the acquisition times of MODIS and CPL measurements. Note that it is very difficult to have time and space coincident aerosol and cloud characterization and vertical distribution. On the other hand, inherent differences among the R_e values retrieved at the various NIR channels can be found due to the vertical distribution of the cloud particle sizes and the different photon transport at the three wavelengths (Platnick, 2000; Platnick et al., 2003). However, in some instances, $R_e(1.6)-R_e(2.1)$ values are found (e.g., in Fig. 10b <-2 μm) that indicate an underestimation of $R_e(1.6)$ that the vertical photon transport alone cannot justify. Only the radiative effect of an overlying aerosol layer can account for this phenomenon.

This study suggests that the use of the 3.7 or 2.1 μm data rather than those at 1.6 μm for the cloud R_e retrieval

is preferable in order to reduce bias in assessing aerosol indirect effect in presence of biomass-burning aerosol. In particular, cloud R_e retrieved at 3.7 μm refer to hydrometeors at cloud top, unlike radii retrieved using the other NIR spectral channels. A difficulty in the use of this channel is the separation of the thermal emitted component from the total signal, but it can be overcome as demonstrated by Nakajima and Nakajima (1995) and King et al. (1997). This result shows once again the effectiveness of the 3.7-μm channel for the R_e retrieval, as also stated by Rosenfeld et al. (2004). However, the 3.7-μm channel, unlike the 2.1-μm one, may be susceptible to errors in the R_e retrievals in the presence of a desert dust aerosol layer overlying a stratocumulus cloud, as demonstrated with radiative transfer simulations in Haywood et al. (2004).

Furthermore, when using satellite-based R_e retrievals, information about the vertical position of aerosol and cloud is required in order to discriminate between the aerosol indirect effect on cloud particle size and the direct radiative effect of an overlying aerosol layer. This task will be performed by the next satellite mission Cloud–Aerosol Lidar and Infrared Pathfinder Satellite Observations (CALIPSO, Winker et al., 2003), which is scheduled for launch in summer 2005. CALIPSO will combine an active lidar instrument (Cloud–Aerosol Lidar with Orthogonal Polarization–CALIOP) with passive IR and VIS imagers to probe the vertical structure and properties of clouds and aerosol on a global scale.

Acknowledgements

MODIS data were made available by the NASA's Earth Science Enterprise. The retrieval algorithms were developed by the MODIS Science Teams. Data were processed by the MODIS Adaptive Processing System (MODAPS) and Goddard Distributed Active Archive Center (DAAC), and are archived and distributed by the Goddard DAAC. The data of the ER-2 Cloud Physics Lidar (CPL) are available on-line at http://cpl.gsfc.nasa.gov/ from the NASA Goddard Space Flight Center, Greenbelt, Maryland, USA. The authors are grateful to the OpenCLASTR project (http://www.ccsr.u-tokyo.ac.jp/~clastr) for developing and making available the package System for Transfer of Atmospheric Radiation (RSTAR). Special thanks go to the AERONET PI B. Holben for the effort in establishing and maintaining the Etosha-Pan site. Three anonymous reviewers deserve recognition for contributing to a significant improvement of the manuscript. This study was funded by EURAINSAT (http://www.isac.cnr.it/~eurainsat), a shared-cost project (contract EVG-1-2000-00030) co-funded by the General Research Directorate of the European Commission within the research and technological development activities of a generic nature of the Environment and Sustainable Development.

References

Ackerman, A.S., Toon, O.B., Stevens, D.E., Heymsfield, A.J., Ramanathan, V., Welton, E.J., 2000. Reduction of tropical cloudiness by soot. Science 288, 1042–1047.

Andreae, M.O., Rosenfeld, D., Artaxo, P., Costa, A.A., Frank, G.P., Longo, K.M., Silva-Dias, M.F., 2004. Smoking rain clouds over the Amazon. Science 303, 1337–1342.

Bréon, F.-M., Tanré, D., Generoso, S., 2002. Aerosol effect on cloud droplet size monitored from satellite. Science 295, 834–838.

Brieglieb, B.P., Minnis, P., Ramanathan, V., Harrison, E., 1986. Comparison of regional clear-sky albedos inferred from satellite observations and model computations. J. Clim. Appl. Meteorol. 25, 214–226.

Cattani, E., Costa, M.J., Torricella, F., Levizzani, V., Silva, A.M., 2003. Comparisons of cloud microphysical properties retrieved from different algorithms during aerosol transport events. Proc. 2003 EUMETSAT Meteorological Satellite Data Users' Conf., Weimar, 29 Sept.–3 Oct, pp. 678–685.

Eck, T.F., Holben, B.N., 1994. AVHRR split window temperature differences and total precipitable water over land surfaces. Int. J. Remote Sens. 15, 576–582.

Eck, T.F., Holben, B.N., Ward, D.E., Mukelabai, M.M., Dubovik, O., Smirnov, A., Shafer, J.S., Hsu, N.C., Piketh, S.J., Queface, A., Le Roux, J., Swap, R.J., Slutsker, I., 2003. Variability of biomass-burning aerosol optical characteristics in southern African during the SAFARI 2000 dry season campaign and a comparison of single scattering albedo estimates from radiometric measurements. J. Geophys. Res. 108 (D13), 8477, doi:10.1029/2002JD002321.

Ellingson, R.G., Ellis, J., Fels, S., 1991. The intercomparison of radiation codes used in climate models: long wave results. J. Geophys. Res. 96 (D5), 8929–8953.

Fu, Q., Liou, K.N., 1992. On the correlated *k*-distribution method for radiative transfer in nonhomogeneous atmospheres. J. Atmos. Sci. 49, 2139–2156.

Garstang, M., Tyson, P.D., Swap, R.J., Edwards, M., Kallberg, P., Lindesay, J.A., 1996. Horizontal and vertical transport of air over southern Africa. J. Geophys. Res. 101, 23,721–23,736.

Grégoire, J.-M., Tansey, K., Silva, J.M.N., 2003. The GBA 2000 initiative: developing a global burned area data base from SPOT-VEGETATION imagery. Int. J. Remote Sens. 24, 1–8.

Haywood, J.M., Osborne, S.R., Francis, P.N., Keil, A., Formenti, P., Andreae, M.O., Kaye, P.H., 2003a. The mean physical and optical properties of regional haze dominated by biomass burning aerosol measured from the C-130 aircraft during SAFARI 2000. J. Geophys. Res. 108 (D13), 8473, doi:10.1029/2002JD002226.

Haywood, J.M., Francis, P.N., Dubovik, O., Glew, M., Holben, B., 2003b. Comparison of aerosol size distribution, radiative properties, and optical depths by aircraft observations and Sun photometers during SAFARI 2000. J. Geophys. Res. 108 (D13), 8471, doi:10.1029/2002JD002250.

Haywood, J.M., Osborne, S.R., Abel, S.J., 2004. The effect of overlying absorbing aerosol layers on remote sensing retrievals of

cloud effective radius and cloud optical depth. Q. J. R. Meteorol. Soc. 130, 779–800.

Holben, B.N., Eck, T.F., Slutsker, I., Tanré, D., Buis, J.P., Setzer, A., Vermote, E., Reagan, J.A., Kaufman, Y.J., Nakajima, T., Lavenu, F., Jankowiak, I., Smirnov, A., 1998. AERONET-A federated instrument network and data archive for aerosol characterization. Remote Sens. Environ. 66, 1–16.

IPCC (Intergovernmental Panel on Climate Change), Climate Change, 2001. In: Houghton, J.T., et al. (Ed.), The Scientific Basis (Contribution of Working Group I to the Third Assessment Report of the Intergovernmental Panel on Climate Change). Cambridge Univ. Press, New York.

Keil, A., Haywood, J.M., 2003. Solar radiative forcing by biomass burning aerosol particles during SAFARI 2000: a case study based on measured aerosol and cloud properties. J. Geophys. Res. 108 (D13), 8467, doi:10.1029/2002JD002315.

Key, J., Schweiger, A.J., 1998. Tools for atmospheric radiative transfer: streamer and FluxNet. Comput. Geosci. 24 (5), 443–451.

King, M.D., Tsay, S.-C., Platnick, S.E., Wang, M., Liou, K.-N., 1997. Cloud retrieval algorithms for MODIS: optical thickness, effective particle radius, and thermodynamic phase. MODIS Algorithm Theoretical Basis Document, No. ATBD-MOD-05, p. 79.

Kistler, R., Kalnay, E., Collins, W., Saha, S., White, G., Woollen, J., Chelliah, M., Ebisuzaki, W., Kanamitsu, M., Kousky, V., van den Dool, H., Jenne, R., Fiorino, M., 2001. The NCEP-NCAR 50-year reanalysis: monthly means CD-ROM and documentation. Bull. Am. Meteorol. Soc. 82, 247–268.

Kneizys, F.X., Shettle, E.P., Abreu, L.W., Chetwynd, J.H., Anderson, G.P., Gallery, W.O., Selby, J.E.A., Clough, S.A., 1988. Users Guide to LOWTRAN 7. AFGL-TR-88-0177.

Lensky, I.M., Rosenfeld, D., 2005. The time-space exchangeability of satellite retrieved relations between cloud top temperature and particle effective radius. Atmos. Chem. Phys. Discuss. 5, 11911–11928.

Levoni, C., Cattani, E., Cervino, M., Guzzi, R., Torricella, F., Di Nicolantonio, W., 2001. Effectiveness of the MS-method for computation of the intensity field reflected by a multi-layer plane-parallel atmosphere. J. Quant. Spectrosc. Radiat. Transfer 69, 635–650.

List, R., 2004. Review and implication of WMO and IUGG recommendations concerning the effect of aerosol pollution and biomass burning on precipitation. Proc. 14th International Conference on Clouds and Precipitation, Bologna (Italy), 19–23 July 2004, pp. 139–145.

Martins, J.V., Tanré, D., Remer, L., Kaufman, Y., Mattoo, S., Levy, R., 2002. MODIS cloud screening for remote sensing of aerosols over oceans using spatial variability. Geophys. Res. Lett. 29, 1619, doi:10.1029/2001GL013252.

McGill, M.J., Hlavka, D.L., Hart, W.D., Scott, V.S., Spinhirne, J., Schmid, B., 2002. Cloud Physics Lidar: instrument description and initial measurement results. Appl. Opt. 41, 3725–3734.

McGill, M.J., Hlavka, D.L., Hart, W.D., Welton, E.J., Campbell, J.R., 2003. Airborne lidar measurements of aerosol optical properties during SAFARI 2000. J. Geophys. Res. 108 (D13), 8493, doi:10.1029/2002JD002370.

Menzel, P., Strabala, K., 2002. Cloud top properties and cloud phase—Algorithm Theoretical Basis Document. Products: 06_L2, 08_D3, 08_E3, 08_M3. ATBD Reference Number: ATBD-MOD-04.

Nakajima, T.Y., Nakajima, T., 1995. Wide-area determination of cloud microphysical properties from NOAA AVHRR measurements for FIRE and ASTEX regions. J. Atmos. Sci. 52, 4043–4059.

Nakajima, T., Tanaka, M., 1986. Matrix formulation for the transfer of solar radiation in a plane-parallel scattering atmosphere. J. Quant. Spectrosc. Radiat. Transfer 35, 13–21.

Nakajima, T., Tanaka, M., 1988. Algorithms for radiative intensity calculations in moderately thick atmospheres using a truncation approximation. J. Quant. Spectrosc. Radiat. Transfer 40, 51–69.

Platnick, S., 2000. Vertical photon transport in cloud remote sensing problems. J. Geophys. Res. 105, 22919–22935.

Platnick, S., King, M.D., Ackerman, S.A., Menzel, W.P., Baum, B.A., Riédi, J.C., Frey, R.A., 2003. The MODIS cloud products: algorithms and examples from Terra. IEEE Trans. Geosci. Remote Sens. 41, 459–473.

Ramanathan, V., Cess, R.D., Harrison, E.F., Minnis, P., Barkstrom, B. R., Ahmad, E., Hartmann, D., 1989. Cloud-radiative forcing and climate: results from the earth radiation budget experiment. Science 243, 57–63.

Rosenfeld, D., 1999. TRMM observed first direct evidence of smoke from forest fires inhibiting rainfall. Geophys. Res. Lett. 26, 3105–3108.

Rosenfeld, D., 2000. Suppression of rain and snow by urban and industrial air pollution. Science 287, 1793–1796.

Rosenfeld, D., Gutman, G., 1994. Retrieving microphysical properties near the tops of potential rain clouds by multispectral analysis of AVHRR data. Atmos. Res. 34, 259–283.

Rosenfeld, D., Lensky, I.M., 1998. Satellite-based insights into precipitation formation processes in continental and maritime convective clouds. Bull. Am. Meteorol. Soc. 79, 2457–2476.

Rosenfeld, D., Cattani, E., Melani, S., Levizzani, V., 2004. Considerations of daylight operation of 1.6-versus 3.7 μm channel on NOAA and METOP satellites. Bull. Am. Meteorol. Soc. 85, 873–880.

Schmid, B., Redemann, J., Russell, P.B., Hobbs, P.V., Hlavka, D.L., McGill, M.J., Holben, B.N., Welton, E.J., Campbell, J.R., Torres, O., Kahn, R.A., Diner, D.J., Helmlinger, M.C., Chu, D.A., Robles-Gonzales, C., de Leeuw, G., 2003. Coordinated airborne, space-borne, and ground-based measurements of massive thick aerosol layers during the dry season in southern Africa. J. Geophys. Res. 108 (D13), 8496, doi:10.1029/2002JD002297.

Stamnes, K., Tsay, S.-C., Wiscombe, W., Jayaweera, K., 1988. Numerically stable algorithm for discrete-ordinate-method radiative transfer in multiple scattering and emitting layered media. Appl. Opt. 27, 2502–2509.

Stein, D.C., Swap, R.J., Greco, S., Piketh, S.J., Macko, S.A., Doddridge, B.G., Elias, T., Bruintjes, R.T., 2003. Haze layer characterization and associated meteorological controls along the eastern coastal region of southern Africa. J. Geophys. Res. 108 (D13), 8506, doi:10.1029/2002JD003237.

Suzuki, K., Nakajima, T., Numaguti, A., Takemura, T., Kawamoto, K., Higurashi, A., 2004. A study of the aerosol effect on a cloud field with simultaneous use of GCM modeling and satellite observation. J. Atmos. Sci. 61, 179–194.

Swap, R.J., Annegarn, H.J., Suttles, J.T., King, M.D., Platnick, S., Privette, J.L., Scholes, R.J., 2003. Africa burning: a thematic analysis of the Southern African Regional Science Initiative (SAFARI 2000). J. Geophys. Res. 108 (D13), 8465, doi:10.1029/2003JD003747.

Torres, O., Bhartia, P.K., Herman, J.R., Ahmad, Z., Gleason, J., 1998. Derivation of aerosol properties from satellite measurements of backscattered ultraviolet radiation: theoretical basis. J. Geophys. Res. 103, 17099–17110.

Twomey, S., 1977. The influence of pollution on the shortwave albedo of clouds. J. Atmos. Sci. 34, 1149–1152.

Twomey, S.A., Piepgrass, M., Wolfe, T.L., 1984. An assessment of the impact of pollution on global cloud albedo. Tellus 36, 356–366.

Winker, D.M., Pelon, J., McCormick, M.P., 2003. The CALIPSO mission: spaceborne lidar for observation of aerosols and clouds. Proc. SPIE 4893, 1–11.

Wiscombe, W.J., 1977. The delta-*M* method: rapid yet accurate radiative flux calculations for strongly asymmetric phase functions. J. Atmos. Sci. 34, 1408–1422.

Wiscombe, W.J., Evans, J.W., 1977. Exponential-sum fitting of radiative transmission functions. J. Comput. Phys. 24, 416–444.

Yamasoe, M.A., Kaufman, Y.J., Dubovik, O., Remer, L.A., Holben, B. N., Artaxo, P., 1998. Retrieval of the real part of the refractive index of smoke particles from Sun/sky measurements during SCAR-B. J. Geophys. Res. 103 (D24), 31893–31902.

Zuberi, B., Johnson, K.S., Aleks, G.K., Molina, L.T., Molina, M.J., Laskin, A., 2005. Hydrophilic properties of aged soot. Geophys. Res. Lett. 32, L01807, doi:10.1029/2004GL021496.